Finite-difference time-domain simulations of exciton-polariton resonances in quantum-dot arrays

Yong Zeng[1,2]**, Ying Fu**[1]**, Mats Bengtsson**[3]**, Xiaoshuang Chen**[2]**, Wei Lu**[2]**, and Hans Ågren**[1]

1. Department of Theoretical Chemistry, Royal Institute of Technology, S-106 91, Stockholm, Sweden

2. National Laboratory for Infrared Physics, Shanghai Institute of Technical Physics, Chinese Academy of Science, 200083 Shanghai, China

3. School of Electrical Engineering, Royal Institute of Technology, SE-100 44, Stockholm, Sweden

fyg@theochem.kth.se, xschen@mail.sitp.ac.cn, luwei@mail.sitp.ac.cn

Abstract: The optical properties of nanosize quantum-dot (QD) arrays are found to vary significantly around the exciton resonance frequency of the QDs. In order to simulate the interactions between electromagnetic waves and QD arrays, a general auxiliary-differential-equation, finite-difference time-domain approach is introduced and utilized in this article. Using this numerical method, the exciton-polariton resonances of single-layer and double-layer GaAs QD arrays are studied. The optical properties of a single-layer QD array are found to be characterized by the Mie resonance of its constituent QDs, while a double-layer QD array is characterized by the quasi-dipole formed by two QDs positioned in each of the two layers.

© 2008 Optical Society of America

OCIS codes: (160.4670) Optical materials; (260.5740) Physical Optics, resonance.

References and links

1. A. V. Zayats, I. I. Smolyaninov, A. A. Maradudin, "Nano-optics of surface plasmon polaritons," Phys. Rep. **408,** 131 (2005).
2. E. Ozbay, "Plasmonics: Merging photonics and electronics at nanoscale dimensions," Science **311,** 189-93 (2006).
3. Y. Fu, M. Willander, E. L. Ivchenko, "Photonic dispersions of semiconductor-quantum-dot-array-based photonic crystals in primitive and face-centered cubic lattices," Superlatt. Microstruct. **27,** 255 (2000).
4. Y. Fu, E. Berglind, L. Thylén, H. Ågren, "Optical transmission and waveguiding by excitonic quantum dot lattices," J. Opt. Soc. Am. B **23,** 2441 (2006).
5. Y. Zeng, Y. Fu, X. Chen, W. Lu, H. Ågren, "Complete band gaps in three-dimensional quantum dot photonic crystals," Phys. Rev. B **74,** 115325 (2006).
6. Y. Zeng, X. Chen, W. Lu, Y. Fu, "Exciton polaritons of nano-spherical-particle photonic crystals in compound lattices," Eur. Phys. J. B **49,** 313 (2006).
7. H. Ajiki, T. Tsuji, K. Kawano, K. Cho, "Optical spectra and exciton-light coupled modes of a spherical semiconductor nanocrystal," Phys. Rev. B **66,** 245322 (2002).
8. H. Ajiki, T. Kaneno, H. Ishihara, "Vacuum-field Rabi splitting in semiconducting core-shell microsphere," Phys. Rev. B **73,** 155322 (2006).
9. H. Mertens, J. S. Biteen, H. A. Atwater, A. Polman, "Polarization-Selective Plasmon-Enhanced Silicon Quantum-Dot Luminescence," Nano Lett. **6,** 2622 (2006).
10. C. Wang, L. Huang, B. A. Parviz, L. Y. Lin, "Subdiffraction Photon Guidance by Quantum-Dot Cascades," Nano Lett. **6,** 2549 (2006).
11. G. Ya. Slepyan, S. A. Maksimenko, V. P. Kalosha, A. Hoffmann, D. Bimberg, "Effective boundary conditions for planar quantum dot structures," Phys. Rev. B **64,** 125326 (2001).

12. O. Voskoboynikov, C. M. J. Wijers, J. L. Liu, C. P. Lee, "Magneto-optical response of layers of semiconductor quantum dots and nanorings," Phys. Rev. B **71,** 245332 (2005).
13. V. Bondarenko, M. Zaluzny, Y. Zhao, "Interlevel electromagnetic response of systems of spherical quantum dots," Phys. Rev. B **71,** 115304 (2005).
14. L. Belleguie, S. Mukamel, "Nonlocal electrodynamics of arrays of quantum dots," Phys. Rev. B **52,** 1936 (1995).
15. X. Zhang, P. Sharma, "Size dependency of strain in arbitrary shaped anisotropic embedded quantum dots due to nonlocal dispersive effects," Phys. Rev. B **72,** 195345 (2005).
16. F. Thiele, C. Fuchs, R. Baltz, "Optical absorption in semiconductor quantum dots: Nonlocal effects," Phys. Rev. B **64,** 205309 (2001).
17. S. Hughes, "Coupled-cavity QED using planar photonic crystals," Phys. Rev. Lett. **98,** 083603 (2007).
18. L. C. Andreani, D. Gerace, M. Agio, "Exciton-polaritons and nanoscale cavities in photonic crystal slab," Phys. Status Solidi B. **242,** 2197 (2005).
19. C. Wang, L. Y. Lin, B. A. Parviz, "Modeling and simulation for a nano-photonic quantum dot waveguide fabricated by DNA-directed self-assembly," J. Sel. Top. Quantum Electron. **11,** 500 (2005).
20. L. Huang, C. Wang, L. Y. Lin, "A comparison of crosstalk effects between colloidal quantum dot waveguides and conventional waveguides," Opt. Lett. **32,** 235 (2007).
21. S. Nojima, "Optical response of excitonic polaritons in photonic crystals," Phys. Rev. B **59,** 5662 (1999).
22. H. Haug, S. W. Koch, *Quantum Theory of the Optical and Electronic Properties of Semiconductors* (World Scientific, Singapore, 1986).
23. R. Zeyher, J. L. Birman, and W. Brenig, "Spatial Dispersion Effects in Resonant Polariton Scattering. I. Additional Boundary Conditions for Polarization Fields," Phys. Rev. B **6,** 4613 (1972)
24. M. Born, E. Wolf, *Principles of optics: electromagnetic theory of propagation, interference and diffraction of light*, Pergamon press 1959.
25. A. Taflove, S. C. Hagness, *Computational Electrodynamics: the finite-difference time-domain method*, Second Edition, Artech House Boston 2000.
26. I. Vurgaftman, J. R. Meyer, L. R. Ram-Mohan, "Band parameters for III-V compound semiconductors and their alloys," J. Appl. Phys. **89,** 5815 (2001).
27. T. Iida, H. Ishihara, "Force control between quantum dots by light in polaritonic molecule states," Phys. Rev. Lett. **97,** 117402 (2006).
28. G. Ya. Slepyan, S. A. Maksimenko, V. P. Kalosha, J. Herrmann, N. N. Ledentsov, I. L. Krestnikov, Zh. I. Alferov, D. Bimberg, "Polarization splitting of the gain band in quantum wire and quantum dot arrays," Phys. Rev. B **59,** 12275 (1999).
29. K. Kempa, R. Ruppin, J. B. Pendry, "Electromagntic response of a point-dipole crystal," Phys. Rev. B **72,** 205103 (2005).
30. J. A. Klugkist, M. Mostovoy, J. Knoester, "Mode Softening, Ferroelectric Transition, and Tunable Photonic Band Structures in a Point-Dipole Crystal," Phys. Rev. Lett. **96,** 163903 (2006).
31. F. J. Taylor, *Principles of signals and systems*, McGraw-Hill, New York, 1994.
32. J. A. Pereda, L. A. Vielva, A. Vegas, A. Prieto, "Computation of resonant frequencies and quality factors of open dielectric resonators by a combination of the finite-difference time-domain (FDTD) and Prony's methods," IEEE Microwave Guid. Wave Lett. **2,** 431 (1992).
33. Y. Hua, T. K. Sarkar, "Generalized pencil-of-function method for extracting poles of an EM system from its transient response," IEEE Trans. Antennas Propag. **37,** 229 (1989).
34. S. Dey, R. Mittra, "Efficient computation of resonant frequencies and quality factors of cavities via a combination of the finite-difference time-domain technique and the Pade approximation," IEEE Microwave Guid. Wave Lett. **8,** 415 (1998).
35. W. Guo, W. Li, Y. Huang, "Computation of resonant frequencies and quality factors of cavities by FDTD technique and Pade approximation," IEEE Microwave and Wireless Components Lett. **11,** 223 (2001).
36. G. A. Baker, *Essentials of Padé approximants*, Academic Press, New York, 1975.
37. V. S. C. Manga Rao, S. Hughes, "Single quantum-dot Purcell factor and β factor in a photonic crystal waveguide," Phys. Rev. B **75,** 205437 (2007).

1. Introduction

Miniaturization and high-density integration constitute important factors in contemporary fabrication of photonic components. The main obstacle for further progress of these factors is governed by the diffraction limit of light, something that has led to a wealth of approaches proposed to circumvent this problem. One of these have concerned the utilization of surface plasmon polaritons, that is coupled polaritons formed by photons and free electrons in a metal [1, 2]. Recently, quantum-dot (QD) arrays have been found to strongly manipulate electromagnetic (EM) waves whose wavelengths are one or two orders of magnitude the radius of the

QDs [3, 4, 5, 6]. For instance, a single-layer array of GaAs/Al$_x$Ga$_{1-x}$As QDs with a radius of 20 nm is found to significantly reflect an EM wave with a wavelength of about 800 nm. The QD-based optical devices could therefore provide a possible approach to decrease the size of devices and further increase the integral density of optical circuits [4, 5]. This possibility has now sparked an abundance of research, both experimentally [7, 8, 9, 10] and theoretically [11, 12, 13, 14, 15, 16, 17, 18, 19, 20].

The underlying physical mechanism of QD-based devices is provided by the exciton-polariton resonances of the QDs [21]. Under an incident EM wave, a confined exciton can be optically excited in the QD. When a photon and an exciton interact in the dispersion-crossover region, a combined quasi-particle, normally known as an exciton polariton, is formed [22]. Because excitons in a macroscopic system spread through the whole structure with an appropriate dispersion, they must be treated with a nonlocal theory [21, 23]. Linear response theory constitutes such a theory, giving the dielectric polarization as

$$\mathbf{P}(\mathbf{r},\omega) = T(\omega)\Phi(\mathbf{r}) \int \Phi(\mathbf{r}')\mathbf{E}(\mathbf{r}',\omega)d\mathbf{r}', \tag{1}$$

where $\Phi(\mathbf{r}) := \Phi(\mathbf{r},\mathbf{r})$ is the ground-state wavefunction of the exciton excited in QD (whose center is denoted by $\mathbf{a}$),

$$\Phi(\mathbf{r}_e,\mathbf{r}_h) = \frac{1}{|\mathbf{r}-\mathbf{a}|\sqrt{2\pi R}} \sin\left(\frac{\pi|\mathbf{r}-\mathbf{a}|}{R}\right) \frac{1}{\sqrt{\pi a_B^3}} e^{-\frac{\mathbf{r}_e-\mathbf{r}_h}{a_B}}. \tag{2}$$

In addition, the coefficient $T(\omega)$ is given by

$$T(\omega) = \frac{2\pi\varepsilon_0\varepsilon_b\omega_{LT}\omega_0 a_B^3}{\omega_0^2 - \omega^2 - 2j\omega\delta}. \tag{3}$$

Here ω_{LT} and a_B are the exciton longitudinal-transverse splitting and Bohr radius in the corresponding bulk semiconductor, respectively. ε_b is the dielectric index of the well material, $j^2 = -1$, δ is a phenomenological parameter describing the decay of single-QD exciton, and R is the radius of the quantum dots. ω_0 is the ground-state exciton resonance frequency of the QDs, which is given by

$$\omega_0 = \frac{E_g}{\hbar} + \frac{\hbar\pi^2}{2m_0 R^2 e}\left(\frac{1}{m_e} + \frac{1}{m_h}\right), \tag{4}$$

when the QD is assumed as a spherical square quantum well. Here E_g is the band gap in the corresponding bulk semiconductor, e is the elementary charge, m_e and m_h are the electronic effective mass and hole effective mass, respectively.

To numerically simulate the interaction between EM waves and QD-based devices, plane-wave-expansion methodologies have frequently been employed. Such an approach was proposed in Ref.[3], and further extended in Ref.[5, 6]. However, it has turned out very difficult to simulate complicated structures and calculate the resonance modes. In this article, we introduce a general auxiliary-differential-equation, finite-difference time-domain (FDTD) approach, which is more powerful and applicable than the original plane-wave-expansion method. This method is further employed for simulations of exciton-polariton resonances in quantum-dot arrays. It should be emphasized that, although the auxiliary-differential-equation FDTD method is very popular in modeling the pulse dynamics of dispersive and nonlinear media, it is the first time, to the best of our knowledge, that this method utilized to simulate quantum dots with nonlocal dielectric polarizations.

Our paper is organized as follows: In Section II we present the numerical calculation method. Numerical results and analysis are presented in Section III. We further discuss our calculation approach and results in Section IV. Section V contains our conclusions.
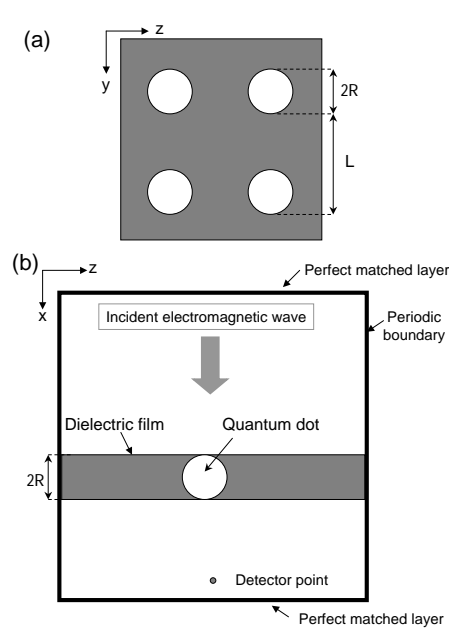
Fig. 1. (a) Schematic drawing of a freestanding dielectric film embedded with a square array of quantum dots. The quantum dot has a radius of R, the square array has a period of L, and the dielectric film has a thickness of $2R$. (b) A cross section of the computational domain consisting of a single unit cell of the quantum-dot array. Periodic boundary conditions are imposed on the four surfaces perpendicular to the dielectric film, while perfect matched layers are imposed at the top and bottom surfaces. The input light wave is polarized along the z direction and propagates to the top dielectric surface along the x direction. The transmitted electric field is collected at the detector point.

2. Calculational method

The interaction between light and nonlocal QDs can be described by the time-dependent Maxwell's equations that are coupled to an equation for the light-induced excitonic polarization current in the QD [24],

$$\nabla \times \mathbf{E} = -\mu_0 \frac{\partial \mathbf{H}}{\partial t}, \quad \nabla \times \mathbf{H} = \varepsilon_0 \frac{\partial \mathbf{E}}{\partial t} + \mathbf{J}, \quad \mathbf{J} = \frac{\partial \mathbf{P}}{\partial t}. \tag{5}$$

Here $\mathbf{E}$ is the electric field vector, $\mathbf{H}$ is the magnetic field vector, $\mathbf{J}$ is a current density corresponding to the nonlocal polarization $\mathbf{P}$ of the QD. To solve the above curl equations, Yee's discretization scheme is here employed [25]. All field variables are defined on a cubic grid. Electric and magnetic fields are temporally separated by one-half time-step and spatially interlaced by half a grid cell. Based on this scheme, center differences in both space and time are applied to approximate Maxwell's equations.

In order to obtain the relation between the current $\mathbf{J}$ and the polarization $\mathbf{P}$, Eq.(1) is rewritten as

$$\mathbf{P}(\mathbf{r}, \omega) = \frac{A}{\omega_0^2 - \omega^2 - 2j\omega\delta} \mathbf{E}_{new}(\mathbf{r}, \omega), \tag{6}$$

where $A = \pi\varepsilon_0\varepsilon_b\omega_{LT}\omega_0$, and the new variable $\mathbf{E}_{new}(\omega)$ is defined as

$$sinc(\frac{\pi|\mathbf{r}-\mathbf{a}|}{R})\int sinc(\frac{\pi|\mathbf{r}'-\mathbf{a}|}{R})\mathbf{E}(\mathbf{r}',\omega)\frac{d\mathbf{r}'}{R^3}, \tag{7}$$

with $sinc(x) = \sin(x)/x$. It should be stressed that the dielectric permittivity of the QD is then very similar to that of a Lorentz-type medium.

Next the polarization current density $\mathbf{J}(\omega)$ is introduced as

$$\mathbf{J}(\mathbf{r},\omega) \equiv -j\omega\mathbf{P}(\mathbf{r},\omega) = \frac{-Aj\omega}{\omega_0^2 - \omega^2 - 2j\omega\delta}\mathbf{E}_{new}(\mathbf{r},\omega), \tag{8}$$

with $j^2 = -1$. Fourier transforming the above equation, its time-domain analog can be written as

$$\omega_0^2\mathbf{J}(t) + 2\delta\frac{d}{dt}\mathbf{J}(t) + \frac{d^2}{dt^2}\mathbf{J}(t) = A\frac{d}{dt}\mathbf{E}_{new}(t). \tag{9}$$

With the discrete time step Δt, and notation $\mathbf{J}^n \equiv \mathbf{J}(n\Delta t)$, a time-difference expression is then found as

$$\mathbf{J}^{n+1} = a_p\mathbf{J}^n + b_p\mathbf{J}^{n-1} + c_p[\mathbf{E}_{new}^{n+1/2} - \mathbf{E}_{new}^{n-1/2}], \tag{10}$$

where

$$a_p = \frac{2 - \omega_0^2\Delta t^2}{1 + \delta\Delta t}, \quad b_p = \frac{\delta\Delta t - 1}{1 + \delta\Delta t}, \quad c_p = \frac{A\Delta t}{1 + \delta\Delta t}. \tag{11}$$

On the other hand, following the Ampere's law,

$$\nabla \times \mathbf{H}(t) = \varepsilon_0\varepsilon_b\frac{d}{dt}\mathbf{E}(t) + \mathbf{J}(t), \tag{12}$$

the finite-difference expression can be written as

$$\mathbf{E}^{n+3/2} = \mathbf{E}^{n+1/2} + \frac{\Delta t}{\varepsilon_0\varepsilon_b}[\nabla \times \mathbf{H}^{n+1} - \mathbf{J}^{n+1}]. \tag{13}$$

Equation 10 with Eq. 13 therefore can be utilized to simulate the nonlocal polarization of the QDs in two steps: (1) From $\mathbf{J}^n$, $\mathbf{H}^n$ and $\mathbf{E}^{n-1/2}$ obtain $\mathbf{E}^{n+1/2}$; (2) From $\mathbf{E}^{n-1/2}$ and $\mathbf{E}^{n+1/2}$ obtain $\mathbf{E}_{new}^{n-1/2}$ and $\mathbf{E}_{new}^{n+1/2}$ and therefore $\mathbf{J}^{n+1}$, meanwhile, from $\mathbf{E}^{n+1/2}$ and $\mathbf{H}^n$ obtain $\mathbf{H}^{n+1}$. Note that the electric field $\mathbf{E}$ is synchronous with $\mathbf{J}$ in Ref.[25] while it here is separated by $\Delta t/2$. Through numerical validation, we found that our equations are stable and effective. Moreover, they can further be in favor of simplifying the following finite-difference expression of the electric field $\mathbf{E}$.

In order to obtain the frequency spectrum as well as the resonance mode, a time-dependent signal is generally transformed into the frequency domain by using discrete Fourier transformation. A detailed description of this transform in FDTD is presented in Appendix A. However, due to that the exciton-polariton resonances of the QD arrays are very sharp, the frequency resolution of the spectrum obtained by the discrete Fourier transform is too poor to distinguish the resonances. We then employ the Padé approximation instead of the discrete Fourier transform to improve the accuracy of the frequency response (Appendix B). Moreover, to alleviate the calculational burden of the Padé approximation, the original time-dependent FDTD output is decimated by a factor of 1/50, to reduce the number of time samples.
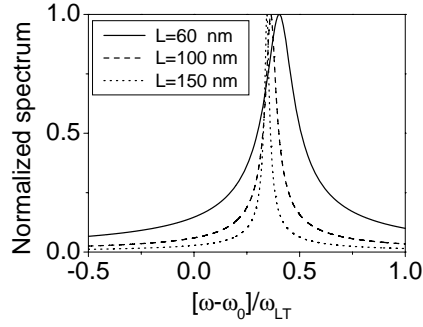
Fig. 2. The normalized amplitude spectra (at the center of the QD) of single-layer quantum-dot arrays with different period L. The dielectric film has a thickness of 40 nm.

3. Results and analysis

The geometry of the system studied computationally is shown in Fig. 1. A freestanding dielectric slab embedded with QD arrays is placed in the middle of the space with its top and bottom surfaces positioned perpendicular to the x direction. Plane waves propagating along the x axis are generated by exciting a plane of identical dipoles in phase. Perfect matched absorbing boundary conditions are applied at the top and bottom of the computational space whereas periodic boundary conditions apply on other boundaries [25]. By placing one unit cell of the periodic QD array in the computational space, we can simulate the temporal transmission of the plane waves normally incident on the QD array which extends infinitely in the y and z directions.

The size of the spatial grid cell Δ is 2 nm in the numerical calculations. The total number of time steps involved in the numerical analysis is 100000 with each time step $\Delta t = \Delta/2c \approx 3.34$ attosecond, where c is the speed of light in vacuum. A time-discrete unit pulse is given as the initial excitation. The dielectric constant of the dielectric slab ε_b is fixed as 12.40, and the square QD array has a period of L in the yz plane. The radius of the QDs is assumed to be uniformly 20 nm. GaAs QDs are considered here. The effective masses of electrons and holes are $m_e = 0.067$ and $m_h = 0.51$, respectively, in the unit of electron rest mass, and the band gap is $E_g = 1.51914$ eV [26]. The corresponding ground-state exciton resonance frequency ω_0 of QDs is then given as 1.535 eV [5]. The exciton longitudinal-transverse splitting ω_{LT} is assumed to be 0.01 eV, and the δ is assumed to be zero.

We first consider the effect of the period L on the resonance frequency of single-layer QD arrays. Three different structures are studied and the amplitude spectra (at the center of the QD) are plotted in Fig.2. In each structure, a strong exciton-polariton resonance is observed around the ground-state exciton resonance of QD. Three important conclusions can be deduced:

(1) The quality factor Q of the exciton-polariton resonance, defined by the ratio between the resonance frequency and its bandwidth $\omega/\Delta\omega$, is very big, indicating a strong localization of the EM field inside the QD array. For instance, Q is about as high as 760 for the structure with $L = 60$ nm. It is for this huge Q that the Padé approximation instead of the discrete Fourier transform is employed in this paper.

(2) The resonance frequency decreases with the increase of L, that is, it is $\omega_0 + 0.404\omega_{LT}$ for $L = 60$ nm, $\omega_0 + 0.363\omega_{LT}$ for $L = 100$ nm, and $\omega_0 + 0.345\omega_{LT}$ for $L = 150$ nm.

(3) The bandwidth of the resonance decreases with the increase of L. This has also been observed from the temporal behavior of the polarization current density $\mathbf{J}(t)$ (the results are not presented here). The amplitude of the current density remains almost unchanged for the
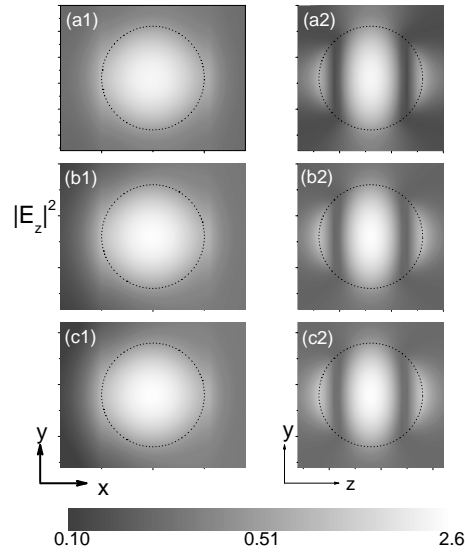
Fig. 3. The distribution of $|E_z^2|$ of single-layer quantum-dot arrays at resonant frequencies, at vertical (x-y plane) cross section and cross section (y-z plane), respectively. (a) $L = 60$ nm and the resonant frequency is $\omega_0 + 0.404\omega_{LT}$. (b) $L = 100$ nm and the resonant frequency is $\omega_0 + 0.363\omega_{LT}$. (c) $L = 150$ nm and the resonant frequency is $\omega_0 + 0.345\omega_{LT}$. The position of quantum dot is marked by dotted lines.

structure with $L = 150$ nm, while it decreases fast for $L = 60$ nm. The transfer of energy stored inside the QD is, therefore, much slower for the larger L.

The above observations can be explained mainly by two facts, (1) the EM field is strongly localized inside the QD but not within the dielectric slab, and (2) the coupling of two neighboring QDs, which can be approximated as dipole-dipole coupling, exponentially decreases with the increase of their interval (the period L). The optical properties of a single-layer QD array is, therefore, mainly determined by its constituent QD. Since the increase of the period L weakens the interaction of the QDs, the resonance frequency of the QD array tends to the Mie resonance frequency of an individual QD, meanwhile, the bandwidth of array decreases to the bandwidth of the Mie resonance of a single QD. Notice that Mie resonance generally means the resonance of a spherical particle under EM radiation. Here we use this term in broader contexts.

To further investigate the underlying physics of exciton-polariton resonances of single-layer QD arrays, the corresponding resonance modes are calculated. The distribution of $|E_z^2|$ at both horizontal (x-y plane) and vertical (y-z plane) cross sections are presented in Fig. 3. Two interesting properties can be observed: (1) the $|E_z^2|$ inside QD increases with the increase of L, due to a diminished coupling between the neighboring QDs; and (2) the EM field is observed to be strongly localized inside the QD. The optical properties of a single QD then significantly affects that of the QD array. Furthermore, the resonance modes for three structures with different L are very similar, indicating an almost identical physical mechanism. This mechanism should be the Mie resonance of an individual QD, as can be observed from the variation of $|E_z^2|$ along the z axis (the polarization direction of the incident light), as plotted in Fig. 4. Two nodes appear at $z = \pm 14$ nm, indicating the formation of a standing wave as well as a resonance along this direction. It is important to point out that this strong localization of visible light inside QD has
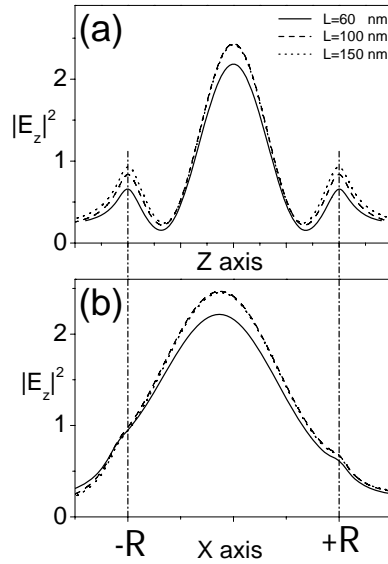
Fig. 4. Variation of $|E_z^2|$ along (a) z axis and (b) x axis including the center of quantum dot, for single-layer quantum-dot arrays with different period L. The position of quantum dot is marked by dash dotted lines.

been already numerically observed and further employed to manipulate collective dynamics of CuCl QD (with a radius of 20 nm) [27].

The experimentally observable transmission spectrum of a single-layer quantum-dot array is also calculated and plotted in Fig.5. The transmission coefficients are almost 100% for frequency far away from the exciton-polariton resonance, while they rapidly drop to almost zero around the resonant frequency. Similar phenomena have been numerically observed in Ref. [4], and an effective classical refractive index of quantum dot has further been employed to explain the dramatic variation of transmission spectrum. More specifically, due to the strong localization of EM field inside quantum dot around the resonance (shown in Fig. 3), the quantum dot phenomenally has a refractive index which is much bigger than that of a non-resonant quantum dot. The light is then almost totally reflected when its frequency is close to the exciton-polariton resonance frequency.

The resonance in a double-layer QD array is here studied using a period of $L = 60$ nm in the $y - z$ plane, and a distance between two identical layers along the x direction (the propagation direction of the incident light) of 40 nm. Its spectrum is plotted in Fig.(6a). As a comparison, the spectrum of the corresponding single-layer array is also presented. Their resonance frequencies are very different: $\omega_0 + 0.726\omega_{LT}$ for the double-layer array, while only $\omega_0 + 0.404\omega_{LT}$ for the single-layer array. Furthermore, the resonance bandwidth of the double-layer structure is much narrower than that of the single-layer array. It should be pointed out that the QDs in the double- and single-layer structures have different local environments, namely QDs in the double-layer are completely embedded in the dielectric while those in the single-layer are not (see Fig.(6b) and Fig.(6c)). We believe that this is the main cause for the difference in the resonant frequencies and bandwidths of the QD arrays.

The resonant mode of such a double-layer array is calculated and the results are plotted in Fig. 7 and Fig. 8. The distribution of $|E_z^2|$ is very similar to that of a dipole in character. The
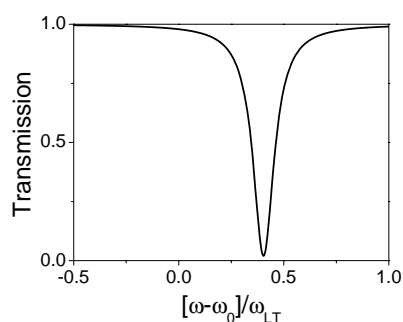
Fig. 5. The transmission spectrum of a single-layer quantum-dot array. The square array has a period of $L = 60$ nm.
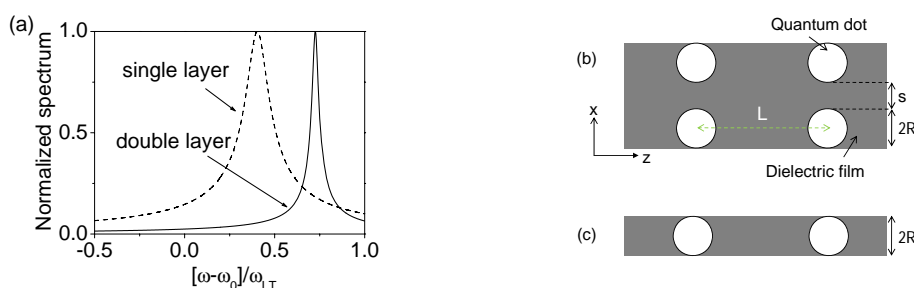

Fig. 6. (a) The normalized spectrum of a double-layer quantum-dot array as well as that of the corresponding single-layer array. The square array has a period of $L = 60$ nm, and the separation between the two layers is $s = 40$ nm. Schematic drawing of a double-layer geometry (b) and a single-layer geometry (c). The quantum dot has a radius of R.

electric field is very strong inside the QD of the first layer, while it is extremely weak inside the QD of the second layer. Furthermore, no nodes have been found in the profile of $|E_z^2|$ along the z axis. The underlying mechanism of the resonances of double-layer arrays are, therefore, very different from the Mie resonance of single-layer arrays. It should be largely determined by the quasi-dipole formed by two QDs, as shown by the resonance mode.

Based on the results presented above, we can conclude that, due to the excitation of exciton polariton, the optical properties of a QD array vary strongly around the ground-state exciton resonance frequency ω_0 of the constituent QDs. For example, if we consider a single array of GaAs/Al$_x$Ga$_{1-x}$As QDs with a radius of 20 nm, the corresponding resonant wavelength is about 800 nm. An electromagnetic wave with a wavelength of about 800 nm will then be significantly manipulated by such a QD array whose thickness is as small as 40 nm. These facts have a bearing on the use of exciton polaritons for beating the diffraction limit of light, and QD arrays of the kind analyzed here may form active constituents in nanoscale photonic circuits and subwavelength components.

4. Discussion

The fact that QD arrays can manipulate strongly EM waves whose vacuum wavelengths are as large as almost two orders of magnitude the QD's radius may suggest the application of
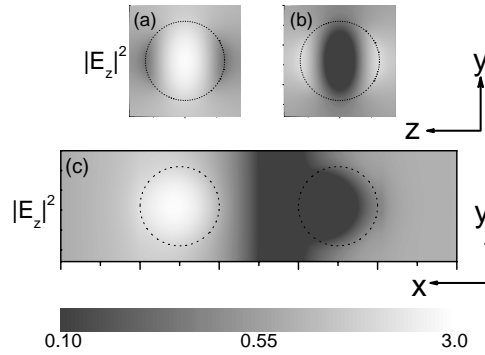
Fig. 7. The distribution of $|E_z^2|$ at a resonant frequency of $\omega_0 + 0.726\omega_{LT}$, at (a,b) cross section (y-z plane) and (c) vertical (x-y plane) cross section, respectively. The double-layer quantum-dot array is same as that in Fig.(6b). The position of quantum dot is marked by dotted lines.
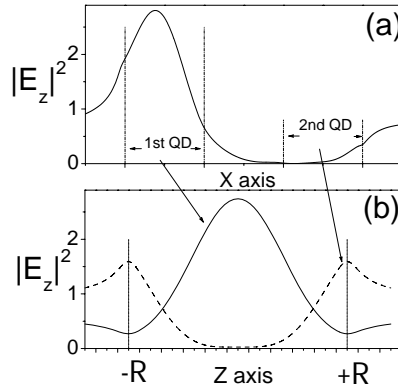

Fig. 8. Variation of $|E_z^2|$ along (a) x axis and (b) z axis including the center of quantum dot. The double-layer quantum-dot array is same as that in Fig.(6b). The position of quantum dot is marked by dash dotted lines.

effective-medium theory. For instance, the Maxwell-Garnett model with the Clausius-Mossotti correction has been utilized to study the polarization splitting of the gain band in QD arrays [28]. In the framework of effective-medium theory, a complex composite material is replaced by a homogeneous medium with effective constitutive parameters. These effective parameters depend upon the generic and the geometrical parameters of the composite material. In other words, the space-dependent dielectric polarization of the original composite material is substituted by the space-independent polarization of the effective homogeneous medium. The EM field accordingly averages over material inhomogeneities. However, as shown in our results, the nonlocal polarization of the QD is very strong around resonance, and so as the EM field inside the QD. Therefore, depolarizing fields, induced by the significant difference between the dielectric constants of the QD and the host semiconductor, must be taken into account in the effective-medium theory. In contrast, the depolarizing field is inherently included in our approach, owing to the application of the exact dielectric polarization **P** (Eq.(1)) of the QD.

We now move on and discuss the relation between our method and the point dipole model [29, 30]. When QD has a dimension much smaller than the wavelength of the EM radiation, and the inter-dot separation was large enough to avoid the wave function overlap, the QD can be approximated as a point dipole centered at its site. In other words, we neglect the spatial dependence of the QD wavefunction, and replace it by a delta function. It should be emphasized that our approach can be modified to simulate point-dipole-model QDs. Consider a QD centered at $\mathbf{r_0}$, replacing its ground-state wavefunction $\Phi(\mathbf{r})$ by delta function $\delta(\mathbf{r} - \mathbf{r_0})$, its dielectric polarization is accordingly simplified as $\mathbf{P}(\mathbf{r}, \omega) = T(\omega)\mathbf{E}(\mathbf{r}, \omega)\delta(\mathbf{r} - \mathbf{r_0})$. Because this simplified polarization has the same characteristics of a point dipole, we can then safely expect that all the physical effects deduced from the point dipole model can be repeated by our method.

Next we discuss the effects of disorder of the QD structures. In our numerical simulations, only ideal systems are considered, that is, the radii of all QDs are assumed to be exactly identical and equal to R, and so the period L. However, certain degrees of structural disorder inevitably exist in actual experiments. The statistic distribution of the sizes of QDs can be described by a Gaussian function centered around R, and so as the resonant frequencies ω_0. Consequently, the structural disorders lead to nonhomogeneous broadenings of the exciton-polariton resonances. The bandwidths of these resonances shown in Fig.2 and Fig.5 should, therefore, be much narrower than that of realistic systems. These resonances may be even completely suppressed when the structural disorders are strong enough.

To close this section we note that the work presented here, a general FDTD method, is just the first part of our whole QD-based-nanophotonics project. Many useful complex structures, such as the coupled QD-photonic-crystal-cavity [17] (and waveguide [37]) systems, will be investigated in the near future by using the numerical method introduced here. Because the optical responses of QDs in our method can be simulated more correctly than by other semiclassical models (the point-dipole model as an example), we believe that the obtained results will be quite important from both fundamental physics and applied perspectives.

5. Conclusion

In conclusion, an auxiliary-differential-equation, finite-difference, time-domain approach is proposed for studies of exciton-polariton resonances in quantum-dot (QD) arrays. The approach is here used to study the effect of the period of the array. Due to the excitation of exciton polaritons, QD arrays are shown to significantly manipulate light with a wavelength around the ground-state exciton resonance of the constituent QDs. The optical properties of a single-layer QD array is found to be largely affected by the Mie resonance of the constituent QDs. On the other hand, the optical properties of double-layer QD arrays is characterized by the quasi-dipole formed by two QDs positioned in each of the two layers. Because the radius of a QD is very smaller than the wavelength of its ground-state exciton resonance, exciton polaritons may offer a solution to the diffraction limit of light, and serve as a basis for constructing nanoscale photonic circuits as well as for the design and fabrication of subwavelength components.

Appendix A: Discrete Fourier Transform

To obtain frequency-domain information, we should transform the temporal response of the finite-difference time-domain (FDTD) simulation to the frequency domain by using a discrete Fourier transform (DFT). Although it is frequently used in FDTD, there exist many conceptual misunderstanding and misuse. Therefore, in the following we describe this transform in detail.

Assuming $\mu(n\Delta t)$ is the time response of one of the six electromagnetic components calibrated from the FDTD technique, its DFT is given by

$$U(N, \omega) = \sum_{n=0}^{N} \mu(n\Delta t) \exp(-in\omega\Delta t), \tag{14}$$

where Δt is the FDTD time interval (also called sampling interval), N is the total time steps used in the simulation, and $i^2 = -1$. If the signal collection time is infinitely long (so that N goes to infinity), we can obtain its discrete-time Fourier transform (DTFT),

$$U(\infty, \omega) = \sum_{n=-\infty}^{\infty} \mu(n\Delta t) \exp(-in\omega\Delta t), \tag{15}$$

which provides an approximation of the continuous-time Fourier transform of a continuous-time function $\mu(t)$

$$U(\omega) = \int_{-\infty}^{\infty} \mu(t) \exp(-i\omega t) dt. \tag{16}$$

According to the Nyquist-Shannon sampling theorem, for a given bandlimited continuous-time signal $\mu(t)$ that is uniformly sampled at a sufficient rate there remains sufficient information in the samples that the original continuous-time signal can be perfectly reconstructed mathematically from only those discrete samples [31]. This holds even if all of the information in the signal between samples is discarded. Considering the calibrated signal $\mu(n\Delta t)$ of the FDTD simulation as an example, if its bandwidth is B, and the sampling interval Δt satisfies

$$B\Delta t < 1, \tag{17}$$

we can reconstruct the original continuous-time signal $\mu(t)$ perfectly from the infinite-length sequences of $\mu(n\Delta t)$ ($n \to \infty$), and further obtain its Fourier spectrum whose frequency resolution is *not limited*. On the other hand, based upon the condition for numerical stability in three-dimensional FDTD, the sampling interval Δt must be bigger than $\Delta x / \sqrt{3}c$, here Δx is the grid size [25]. It is therefore very easy to satisfy the limitation $B\Delta t < 1$ in our FDTD calculation.

However, it is impossible to collect an infinite-length sampled signal in a realistic FDTD simulation, and we can only obtain a finite-length $\mu(n\Delta t)$ with $n \leq N$. According to the uncertainty principle, this finite sampling time duration results in an inadequate frequency resolution in the corresponding Fourier spectrum, which is reciprocal to $N\Delta t$ [31]. Thus, to achieve a reasonable frequency resolution, it is necessary to run the simulation for a sufficiently long time.

Now let us estimate the total number of time steps N needed in our quantum dot (QD) simulation. It is known that the optical properties of QDs vary intensively in a narrow frequency region $[\omega_0 - \omega_{LT}, \omega_0 + \omega_{LT}]$, where ω_0 and ω_{LT} are the QD's exciton resonance frequency and exciton longitudinal-transverse splitting, respectively [3, 4, 5, 6]. It should be stressed that the ratio ω_0/ω_{LT} of a realistic QD is generally as high as 10^4. Even for a frequency resolution as $\omega_{LT}/20$, with a coarse grid size $\lambda/20 = \pi c/10\omega_0$, the total number of time steps N has to be as large as 10^6, i.e., $100\omega_0/\omega_{LT}$. Therefore, the calculational burden is extremely huge.

Appendix B: Padé Approximation

When simulating high quality-factor cavities with the FDTD technique, many parametric model based approaches have been proposed to alleviate the limited frequency resolution of the discrete Fourier transform (DFT), including the Prony's method[32], the generalized pencil-of-function method [33] and the Padé approximation [34, 35, 36]. Following the algorithm presented in [34, 35, 36], we here briefly describe the Padé approximation in the language of classical signals and systems.

The spectral response $P(\omega)$ of the calibrated time-domain data $\mu(n\Delta t)$ is generally obtained by,

$$P(\omega) = \sum_{n=0}^{N} \mu(n\Delta t) \exp(-in\omega\Delta t) \tag{18}$$

This $P(\omega)$ can be further represented by a sum of pole series

$$P(\omega) = P_p(\omega) + P_{np}(\omega), \tag{19}$$

where the term $P_p(\omega)$ contains all the poles of $P(\omega)$, and $P_{np}(\omega)$ represents the remainder. However, the frequency resolution of $P(\omega)$ is obstructed by the uncertainty principle discussed in Appendix A.

To improve the accuracy of the frequency response, the recursion-scheme diagonal Padé approximation is employed instead of the DFT to obtain the spectral response. We assume $P(\omega) \approx P_p(\omega)$ can be approximated by a rational function

$$P(\omega) = \left[\frac{\eta_N(z)}{\theta_N(z)}\right]_{z=e^{-i\omega\Delta t}}, \tag{20}$$

where N is assumed as an even number. The numerator and denominator polynomials, $\eta_N(z)$ and $\theta_N(z)$, are given by

$$\eta_N(z) = \sum_{n=0}^{N} \alpha_n z^n, \quad \theta_N(z) = \sum_{n=0}^{N} \beta_n z^n. \tag{21}$$

In order to obtain the unknown coefficients α_n and β_n, a recursion scheme is used [36]. Two sequences $\eta_j(z)$ and $\theta_j(z)$ are introduced, and they satisfy the following recursion relation,

$$\begin{aligned}
\eta_{2j}(z) &= \eta_{2j-2}(z) - \frac{z\eta_{2j-1}(z)\bar{\eta}_{2j-2}}{\bar{\eta}_{2j-1}}, \quad \theta_{2j}(z) = \theta_{2j-2}(z) - \frac{z\theta_{2j-1}(z)\bar{\eta}_{2j-2}}{\bar{\eta}_{2j-1}}, \\
\eta_{2j+1}(z) &= \frac{\bar{\eta}_{2j}\eta_{2j-1}(z) - \bar{\eta}_{2j-1}\eta_{2j}(z)}{\bar{\eta}_{2j} - \bar{\eta}_{2j-1}}, \quad \theta_{2j+1}(z) = \frac{\bar{\eta}_{2j}\theta_{2j-1}(z) - \bar{\eta}_{2j-1}\theta_{2j}(z)}{\bar{\eta}_{2j} - \bar{\eta}_{2j-1}},
\end{aligned} \tag{22}$$

where $\bar{\eta}_j$ is the coefficient of the highest power of z in $\eta_j(z)$, that is, $z^{N-\lfloor (j+1)/2 \rfloor}$. In addition, the starting values are given by

$$\eta_0(z) = \sum_{n=0}^{N} \mu(n\Delta t)z^n, \quad \eta_1(z) = \sum_{n=0}^{N-1} \mu(n\Delta t)z^n, \tag{23}$$

and $\theta_0(z) = \theta_1(z) = 1$.

Clearly, in Eq. 20, $P(\omega)$ is given by $\eta_0(e^{-i\omega\Delta t})/\theta_0(e^{-i\omega\Delta t})$, whereas the Padé approximation is $\eta_N(e^{-i\omega\Delta t})/\theta_N(e^{-i\omega\Delta t})$. It should be stressed that the original time-dependent FDTD output $\mu(n\Delta t)$ is usually decimated to result in a shorter sequence to save the calculational burden of the Padé approximation. The total number N of time steps in the FDTD, may therefore be larger than the N used in Eq. 20.